

Fully 3D-Printed Cuff Electrode for Small Nerve Interfacing

Francisco Zurita, Leroy Grob, Amelie Erben, Fulvia Del Duca, Hauke Clausen-Schaumann, Stefanie Sudhop, Oliver Hayden, and Bernhard Wolfrum*

Interfacing with the peripheral nervous system is a powerful method for diagnosing and treating several diseases, such as drug-resistant epilepsy and depression. In most clinical applications, large nerves such as the vagus and the hypoglossal nerve are targeted. Large nerves carry multiple nerve fibers, and maintaining selectivity of a specific target response demands complex stimulation strategies. As the large trunks bifurcate toward their distal ends, their diameter and number of comprised fibers reduce. Consequently, interfacing small nerves can provide increased fiber selectivity. However, their small size presents challenges to the fabrication and implantation of suitable electrodes due to their fragility and constrained environments. Here, a cuff electrode that combines two-photon stereolithography and 3D inkjet printing techniques for the selective interfacing of small nerves *in vivo* is introduced. The device is easy to implant, and its size can be tailored for specific nerve dimensions. Its capability to record and selectively stimulate is demonstrated by targeting a locust's hind leg nerve.

body functions. For instance, the stimulation of the vagus nerve to treat epilepsy, and depression is already clinically applied.^[1,2] Current research shows that the activity of the vagus nerve could also be modulated to treat inflammatory bowel disease,^[3] obesity,^[4] and even respiratory symptoms associated with COVID-19.^[5] Furthermore, there is ongoing research on the applicability of peripheral nerve interfaces to provide sensory feedback for prostheses.^[6,7] All these applications commonly target the larger nerves of the body that comprise multiple nerve fibers, and their stimulation often elicits undesired side effects.^[8] Different approaches and techniques have been developed to increase fiber selectivity during nerve stimulation.^[9] Invasive intra-neural interfacing methods achieve a higher selectivity by placing the electrodes inside the

1. Introduction

Interfacing with the peripheral nervous system has a high potential for diagnosing and treating diseases and regulating

nerve.^[10–12] However, such invasiveness can lead to foreign body reactions, which are problematic for long-term implantations.^[13] Extra-neural electrodes interface with the nerves without penetrating them but have a reduced spatial resolution, as they are only in contact with the surface of the nerve.^[14,15] Increasing the number of electrode sites is a common strategy to partially overcome these limitations.^[16]

F. Zurita, L. Grob, F. Del Duca, B. Wolfrum
Neuroelectronics

Munich Institute of Biomedical Engineering
Department of Electrical Engineering
School of Computation, Information and Technology
Technical University of Munich
Hans-Piloty-Str. 1, 85748 Garching, Germany
E-mail: bernhard.wolfrum@tum.de

A. Erben, H. Clausen-Schaumann, S. Sudhop
Center for Applied Tissue Engineering and Regenerative Medicine
Munich University of Applied Sciences
Lothstr. 34, 80533 Munich, Germany

A. Erben, O. Hayden
Heinz-Nixdorf-Chair of Biomedical Electronics
TranslaTUM, Campus Klinikum rechts der Isar
School of Computation, Information and Technology
Technical University of Munich
Einsteinstraße 25, 81675 Munich, Germany

 The ORCID identification number(s) for the author(s) of this article can be found under <https://doi.org/10.1002/admt.202200989>.

© 2022 The Authors. Advanced Materials Technologies published by Wiley-VCH GmbH. This is an open access article under the terms of the Creative Commons Attribution License, which permits use, distribution and reproduction in any medium, provided the original work is properly cited.

A complementary method to increase selectivity and limit undesired side effects is to interface smaller nerves comprising fewer axons. As small nerves in humans can scale down to double-digit micrometers, materials and techniques used to fabricate electrodes have to be refined in size, flexibility, and stiffness to ensure the vitality of these delicate structures during interfacing.^[9,17] Commercially available cuff electrodes can interface with small nerves in the range of 100 μm in diameter and below (e.g., CorTec GmbH, Freiburg, Germany, MicroProbes, Gaithersburg, MD, USA). However, the overall dimension of these devices is usually much larger due to fabrication constraints (around 10 \times for inner diameters of 100 μm), which often proves inconvenient for implantation due to space restrictions. In addition to size, the difficulty of interfacing is a common practical limitation. Most cuff electrodes require buckling or stitching the structure around the nerve, which often demands a high degree of skill from the practitioner.

The fabrication of suitable cuff electrodes has been enhanced in the last years with the incorporation of additive manufacturing technologies to rapidly prototype cost-effective novel devices and sensors. As a result, 3D-printed microscale devices have been fabricated for electrical stimulation.^[18] In particular,

DOI: 10.1002/admt.202200989

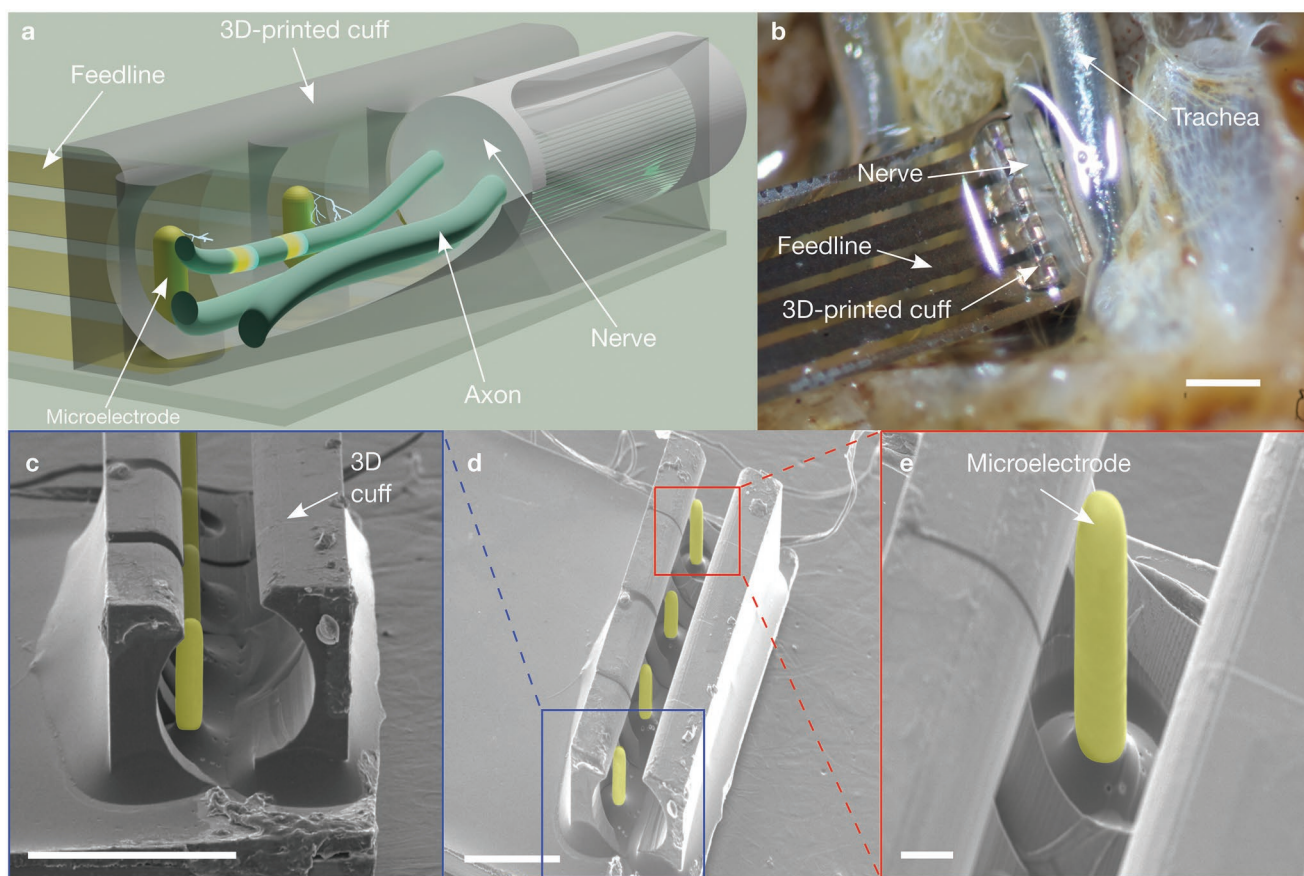


Figure 1. Nerve interfacing with the 3D printed cuff electrode. a) Concept image of a nerve with three axons, interfaced with our designed cuff electrode. The nerve is only shown along half the length of the cuff electrode for a better view of the axons and 3D microelectrodes. b) Microscopy image of the cuff electrode wrapping around a nerve (N5) of a locust. The scale bar corresponds to a length of 500 μm . c–e) Tilt-corrected scanning electron microscope images of the fabricated cuff electrode. A substrate tilt of 45° (d,e), and 70° (c) were used to image the cuff electrode. The 3D electrodes have been false-colored in yellow for clarity. All 3 images were taken using an accelerating voltage of 15 kV. The scale bars shown in each image correspond to a length of 300 (c, d) and 40 μm (e).

two-photon stereolithography (TPS) is one of the few techniques that is capable of fabricating free-form structures at sub-micron accuracy.^[19,20] Previous studies on TPS-fabricated devices for electrical stimulation include alignment tools to assemble carbon fiber electrodes,^[21] microscaffolds for drug loading accompanying flexible electrode arrays for cochlear insertions,^[22] free-standing microelectrodes with carbon electro-active surfaces,^[23] as well as electrode-laden nanoclips capable of interfacing with nerves >50 μm in diameter.^[24,25] These studies have achieved the measurements of spontaneous multiunit activity, stimulation-evoked compound responses,^[21] auditory brain stem responses,^[22] in vivo dopamine response,^[23] and nerve activity.^[24–26]

This article proposes an additively manufactured, multi-channel cuff electrode for interfacing with micrometer-sized nerves that can stimulate and record neural activity. We combine inkjet-printed 3D microelectrodes and TPS-printed 3D cuffs to produce the interfacing devices. Our 3D microelectrodes function as active sites, while 3D-printed cuffs provide mechanical attachment to small nerves. In contrast to previous devices that combine photolithographic methods with TPS, inkjet printing permits rapid prototyping of 3D electrodes

by reducing the number of fabrication steps and the lack of need for a cleanroom. Additionally, we show the stimulation and recording capabilities of the proposed electrode in a locust model. This multisite design can evoke different neural responses when used with the appropriate stimulation patterns.

2. Results and Discussion

Peripheral nerve interfacing is often performed in large nerves in mammals, such as the sciatic nerve of rats ($\varnothing \approx 1 \text{ mm}$). However, small-nerve interfacing requires the implementation of an equally small interfacing electrode, which presents two challenges: the fabrication of the small electrode and a delicate interfacing procedure. Therefore, we developed a small cuff electrode with a straightforward interfacing mechanism, depicted conceptually in **Figure 1a**. With this design, the interfacing is accomplished by simply sliding the nerve inside the cuff opening. Furthermore, we demonstrate the capability of our device to interface insect nerves of $\approx 150 \mu\text{m}$ in diameter in only $\approx 1 \text{ mm}$ of nerve length (Figure 1b). Figure 1c–e shows scanning electron microscope images of the cuff electrode

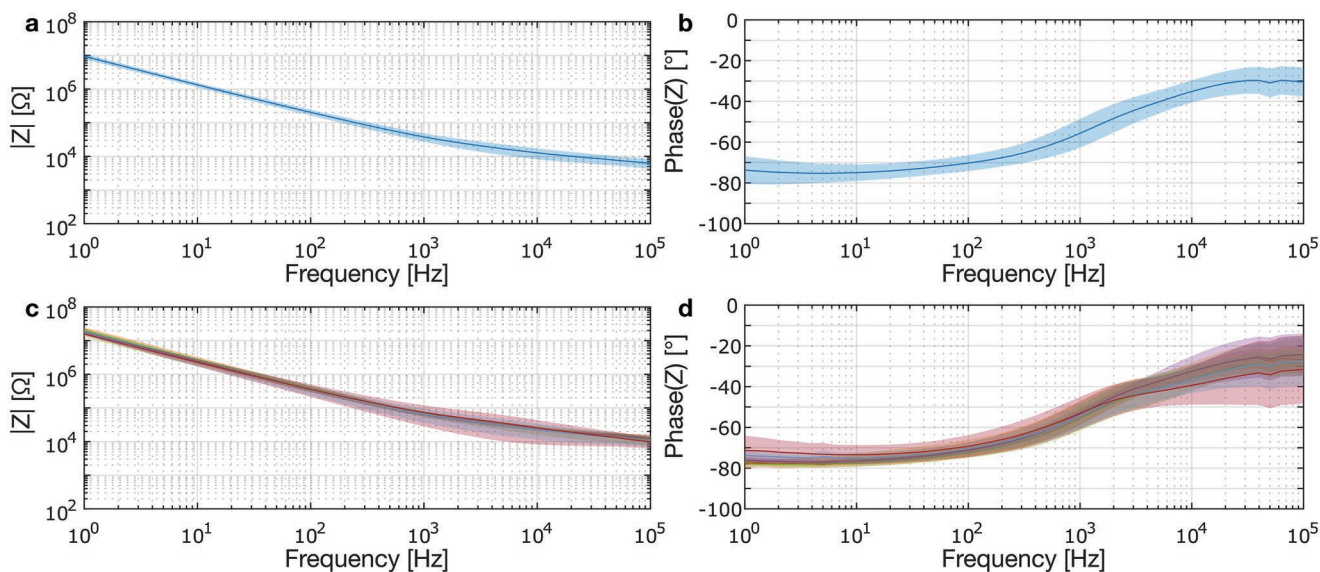


Figure 2. Electrochemical impedance spectroscopy characteristics of the electrode. a,c) Magnitude and b,d) phase of the impedance of differently configured 3D electrodes in locust saline. Averaged impedance data between 3D electrodes and a Pt mesh in (a) and (b) ($n = 16$). Averaged impedance data between two 3D electrodes measured against each other in different configurations in (c) and (d) ($n = 3-5$).

devices, showcasing the electrodes (yellow false-colored), the 3D printed cuff, and the cavity to insert the nerve. They present an estimated geometric surface area of $\approx 0.02 \text{ mm}^2$.

2.1. Electrochemical Characterization of the Electrodes

Impedance measurements were conducted in locust Ringer solution to investigate the electrochemical behavior of the printed electrodes for stimulation. The measurements were performed in a 2-electrode configuration to characterize the impedance of the system as a whole. First, we evaluated the performance of each individual electrode against a platinum electrode serving as combined counter and reference electrode. The exposed surface of the counter electrode was several orders of magnitude larger than the actual working electrode to avoid significant voltage drops at the in the two-electrode configuration. Afterward, we repeated this measurement between individual electrodes, since the stimulation signal is applied in this configuration. **Figure 2a,b** shows the impedance between each individual 3D electrode and a combined counter and reference Pt mesh electrode, showcasing an impedance magnitude of $\approx 30 \text{ k}\Omega$ @ 1 kHz. **Figure 2c,d** shows the impedance between two individual 3D electrodes, one set as the working electrode and the other as the combined counter and reference electrode. The impedance between individual electrodes increases by a factor of ≈ 2 compared to the first setup, which is expected as the Pt mesh electrode presents a lower impedance due to its larger surface area.

2.2. Stimulation Results

The N5 is a nerve that comprises fibers responsible for the fast tibiofemoral angle extension of the locust's hind leg in

movements like jumping and kicking. We interfaced our cuff electrodes with this nerve to validate its stimulation capabilities. The elicited motion of the hind leg of the locust was captured on camera.

Initially, we investigated the influence of the number of stimulation pulses on the observed leg extension using only 2 out of the 4 individual electrodes to assess movement using the simplest electrode configuration. In this configuration, the biphasic stimulation threshold that needs to be delivered to perceive movement was found to be $24 \mu\text{A}$, 500 μs phase duration, which corresponded to a light twitching movement. To reliably elicit measurable leg extension, we applied a stimulus signal using a train of 1 kHz, 60 μA biphasic pulses (3 mA mm^{-2} estimated current density). Each phase was 500 μs long, and each train comprised 5 to 20 individual pulses. The pulse trains were delivered every 1 s, at $t = 0$. The response to the different stimulation patterns is depicted in **Figure 3a,b**. The movement traces corresponding to other combinations can be found in the Supporting Information. Each trace exhibits the mean and standard deviation of the angle variation of the tibiofemoral joint of the leg elicited by the stimulation signal ($n = 20$). The electrodes used are shown in red (leading cathodic phase) and light blue (leading anodic phase). The unused electrodes are shown in black. The 6 possible combinations were tested, and leg movement was elicited in all of them. Since the angle span caused by the stimulation depended on the initial position of the leg, we considered the joint angle span from the moment the leg returned to a similar initial position. While the initial angle varied within the experiment, we observed a tendency for lower maximum leg extension and faster retraction when applying only 5 pulses as opposed to higher pulse numbers. We further investigated the influence of pairing different electrodes on the elicited leg response using four stimulation electrodes simultaneously. To assess the geometric influence of the electrode configuration

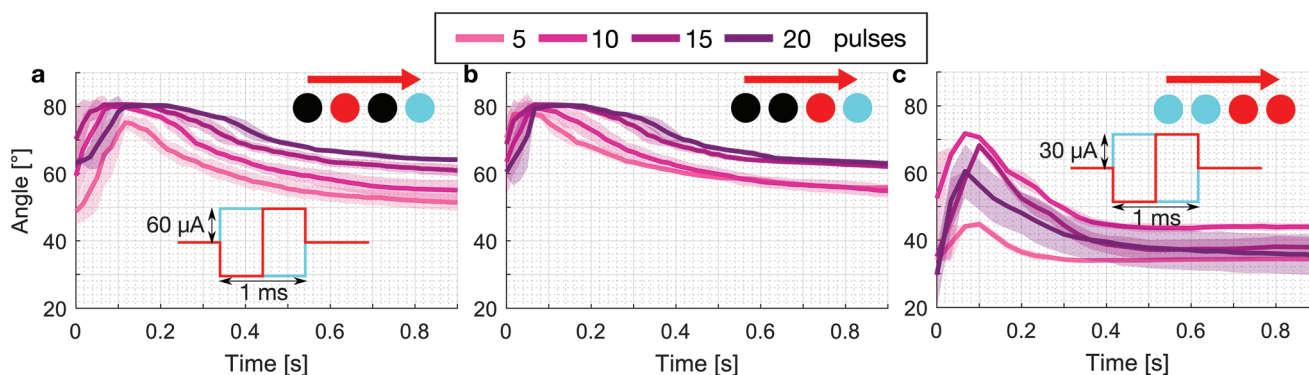


Figure 3. Tibiofemoral joint angle span elicited through electrical stimulation. Different electrode combinations were used, with a leading cathodic phase (red), a leading anodic phase (light blue), and inactive electrode (black). The red arrow indicates the proximal-to-distal direction of the nerve relative to the electrodes. The stimulation current was a sequence of bipolar pulses in succession starting at $t = 0$, shown in (a) and (c). a,b) The stimulus is a bipolar current pulse train of $60 \mu\text{A}$ of amplitude and $500 \mu\text{s}$ pulse duration between two individual electrodes. The number of delivered pulses ranges from 5 to 20, and each trace shows the mean and standard deviation of 20 stimulation events. c) The stimulus is a bipolar current pulse train of $30 \mu\text{A}$ of amplitude and $500 \mu\text{s}$ pulse duration between two pairs of electrodes. For this last scenario, movement was elicited when both phases were on adjacent electrodes. For all other combinations of pairs of electrodes, no movement was elicited.

on the elicited movement response, always two electrodes were set on the same phase while all electrodes delivered the same stimulating current magnitude. Each electrode delivered 1 kHz , $30 \mu\text{A}$ biphasic pulses to keep the total delivered current per phase the same as in the previous experiment (1.5 mA mm^{-2} estimated current density). Figure 3c shows the result for a combination of both leading cathodic (“C”) and anodic (“A”) phases on the same end of the cuff electrode (“AACC”). A similar result was achieved by inverting the leading phases for this case (“CCAA”). However, for all other combinations of “C” and “A,” no movement was elicited. To exclude the possibility that the lack of absolute injected charge causes the absence of a response, we increased the number of pulses up to 100, to no avail (data not shown). However, an increase in current amplitude to $35 \mu\text{A}$ and, therefore, an increased charge per phase, elicited leg movement again with only 5 pulses. Further increasing the current amplitude decreases the elicited angle span because the average final position of the leg approaches its full extension. This phenomenon can be attributed to the stronger depolarization caused by tetanic contraction, making the contraction last longer.^[27] While both stimulation protocols (using 2 or 4 electrodes) delivered the same charge, movement could not be elicited for some combinations, suggesting that the electrode configuration influences the stimulation pattern.

2.3. Simulation of Activating Function

To investigate the influence of the electrode configuration on the activating function, we performed finite element method simulations with COMSOL Multiphysics (COMSOL AB, Stockholm, Sweden). The activating function f_x for extracellular nerve stimulation along the fiber length coordinate x is proportional to the second spatial derivative of the extracellular potential along the fiber $f_x \propto d^2V/dx^2$.^[28] Since the electric field is related to the electric potential by $\mathbf{E} = -\nabla V$, the activating function can be expressed as $f_x \propto -dE_x/dx$. In the

following, we refer to the normalized activating function $f_{n,x} = -dE_x/dx$, disregarding the proportional factor because we are only interested in a comparative analysis. Given a medium with conductivity σ , the electric field \mathbf{E} is related to the current density \mathbf{j} following Ohm’s law $\mathbf{j} = \sigma\mathbf{E}$. Therefore, the applied stimulation current modulates the electric field and, consequently, the activating function along the nerve. The microelectrodes, the 3D-printed nerve cuff, and locust saline solution were modeled using material properties of Ag ($\sigma = 6.3 \times 10^7 \text{ S m}^{-1}$), insulating material, and PBS electrolyte solution ($\sigma = 1.52 \text{ S m}^{-1}$), respectively. The nerve was modeled as a cylinder ($r = 80 \mu\text{m}$, $\sigma = 0.57 \text{ S m}^{-1}$ in the direction along the axon, 0.083 S m^{-1} in the other two directions) surrounded by a nerve sheath ($d = 10 \mu\text{m}$, $\sigma = 2.1 \times 10^{-3} \text{ S m}^{-1}$),^[29] as shown in Figure 4a. The nerve comes in contact with the electrode at a height where the horizontal (xy) plane crosses the center of the nerve. Further information on the simulation conditions can be found in the Supporting Information.

The longitudinal component of the electric field E_x was computed for two electrode configurations, CCAA and CACA, where again “C” stands for a cathodic stimulation pulse, and “A” for an anodic stimulation pulse. Figure 4b,c shows E_x on a plane parallel to the base of the cuff that cuts through the middle of the nerve for CCAA and CACA, respectively (top view). It can be seen that E_x reaches higher values for CCAA than for CACA, suggesting that the electrode phase influences E_x . Then, we computed E_x and the activating function along the center of the nerve for CCAA and CACA, and the results are shown in Figure 4d,e, respectively. The activating function has a higher amplitude for CCAA than for CACA, suggesting that the CCAA configuration is more likely than the CACA configuration to elicit a neural response given the same stimulation amplitude, which is in line with the observed behavior. Furthermore, the obtained activating function values for comparable injected charge are similar to those reported in the literature.^[30] These results suggest that spatial selectivity is possible by modulating the stimulation current and generating the desired activating function.

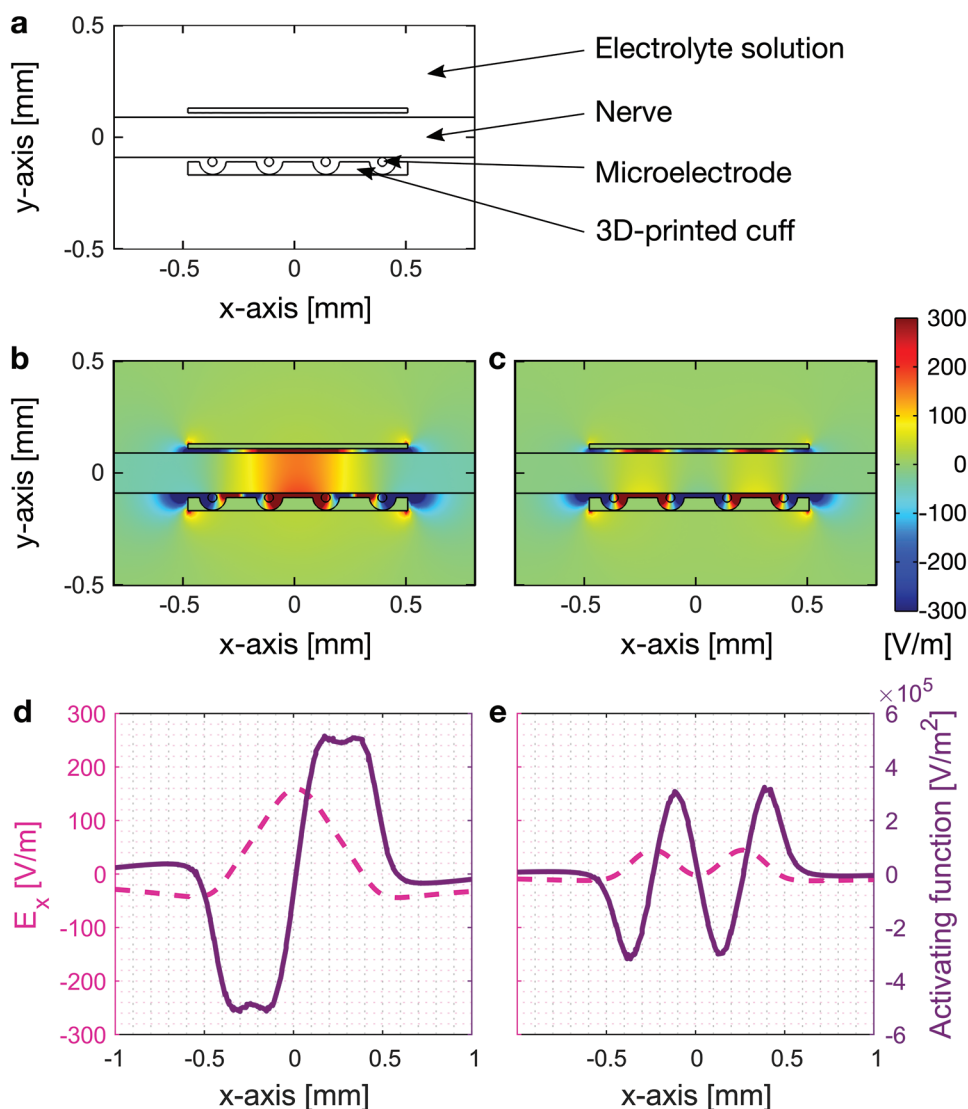


Figure 4. Finite-element-method simulations of the electric field and activating functions for two electrode configurations. a) Top view of the simulated elements on a plane cutting through the middle of the nerve, perpendicular to the microelectrodes. E_x component of the electric field for b) CCAA and c) CACA configurations. E_x component and activating function along the center line of the nerve ($y = 0$) for d) CCAA and e) CACA configurations.

2.4. Recording of Neural Activity

The N5 comprises nerve fibers that convey sensory information to the metathoracic ganglion (afferent) or motor signals from the ganglion to the leg (efferent). We elicited movement (see Experimental Section) and recorded activity of the nerve on all electrodes to validate the ability of our device to detect electrophysiological signals. The average noise floor of all channels was $11.7 \mu\text{V}_{\text{rms}}$. The acquired neural signals presented a phase delay between electrodes, only found in two combinations: from ch1 to ch4 and from ch4 to ch1 (ch1 being the most proximal electrode to the ganglion and ch4 the most distal). Since no other phase combination was found, we believe this lag can be attributed to the propagation velocity of both efferent (ch1 to ch4) and afferent (ch4 to ch1) neural signals. **Figure 5** shows the mean and standard deviation for 50 occurrences of each signal propagation event. These results demonstrate our

cuff electrode's capability to distinguish between afferent and efferent nerve fiber activity. Given the time difference between the peak of the pulses from channels 1 to 4, and knowing that the distance between them corresponds to $768 \mu\text{m}$ by design, we estimated a mean conduction velocity of 3.47 and 0.88 m s^{-1} standard deviation. Furthermore, the delay estimation does not distinguish between individual nerve fibers, which means that the spikes recorded could correspond to compound action potentials (CAPs). CAPs comprise multiple fibers' activity and last longer than individual action potentials, which could introduce errors when estimating the propagation velocity. Conduction velocities previously reported in the literature on motor fibers found in the crural nerve of the locust range from 1.6 to 2.3 m s^{-1} .^[31] To the best of our knowledge, there are no reports on localized conduction velocity of the N5 at a close distance to the ganglion. Phase measurements could be used, for example, for the detection or evaluation of neurodegenerative

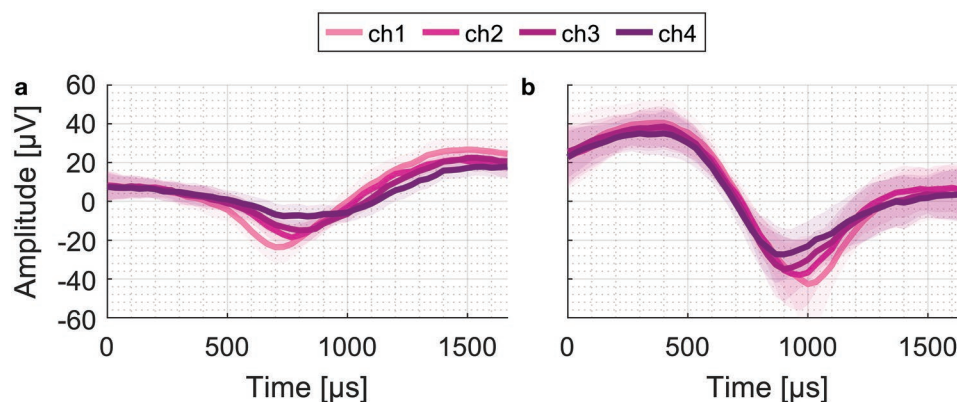


Figure 5. Mean and standard deviation for $n = 50$ compound action potential events. a) The phase of the channels leads in proximal (ch1) to distal (ch4) direction, hinting activity from efferent nerve fibers. b) The phase of the channels leads in distal (ch4) to proximal (ch1) direction, hinting activity from afferent nerve fibers.

diseases that affect the action potential propagation velocity along the nerve, like multiple sclerosis,^[32] or to extract features to increase the recording selectivity using neural networks.^[33]

Although we were able to record neural activity with our device, the SNR achieved is low due to the imperfect electrical sealing of the individual electrodes.^[34,35] This incomplete sealing derives from the unsuccessful polymerization of the resin at the interface of the individual electrodes, and it occurs when the laser used for two-photon stereolithography is focused in their vicinity (refer to the Supporting Information). This effect is most likely due to the absorption characteristics of Ag (between 350 and 500 nm) at the laser's wavelength (780 nm), which results in a reflection of the light. This reflection results in an overexposure of the resin, creating bubbles that prevent its correct polymerization. To improve the electrode sealing, a non-metallic conductor, such as PEDOT:PSS, could be used as the material for the 3D microelectrodes.^[36,37] This material would potentially improve the polymerization around the 3D microelectrodes, given its energy absorption characteristics at wavelengths above 310 nm.^[38] Furthermore, a PEDOT:PSS coating would reduce the electrode voltage generated during stimulation, preventing the occurrence of undesired electrochemical reactions.^[39]

The importance of proper sealing for nerve interfacing becomes clear when we compare our device with standard hook electrode recordings (see Figure S7, Supporting Information). Pulling the nerve out of the hemolymph with Ag hook electrodes, typically results in an improvement of both, stimulation and recording, due to the reduction of leakage current through the external electrolyte. However, when the hook electrodes are immersed in the electrolyte (comparable to an in vivo configuration), the stimulation and recording performance degrades drastically due to lack of electrical insulation between the electrodes. In such a configuration, no action potentials were visible during recording with immersed hook electrodes.

Similarly, in our previous work, we interfaced the N5 with custom Ag electrodes within a silicone cuff.^[40] While stimulation was possible with such a device, recording of activity was not successful, probably due to an insufficient sealing at the planar Ag electrode surface. In contrast to the hook electrode and planar cuff electrode, the printed 3D cuff electrode device

was able to stimulate and record from the N5 when immersed in the electrolyte.

Future improvements should address concepts for fast implantation procedures without risking damage to the nerve structure as well as possibilities for long-term application. Although silver is widely used in electrophysiological measurement, it is not recommended for long-term use, due to known biocompatibility issues. A potential improvement in this regard could be gained by electroplating the 3D electrodes with Au or Pt^[41] or conductive polymers, such as PEDOT:PSS, which has been shown to achieve low cytotoxicity and high electrochemical stability.^[42,43]

3. Conclusion

In this article, we present a novel, entirely additively manufactured, 3D cuff electrode for small nerve interfacing. The individual electrodes are made of inkjet-printed Ag, whereas the cuffing mechanism is 3D printed around the electrodes using two-photon stereolithography. Our device offers a straightforward mechanical attachment with the nerve. We demonstrate successful stimulation and recording of a locust nerve involved in the fast tibiofemoral joint extension. Different combinations of electrodes, stimulation amplitude, and phase can be used to elicit different movement patterns on the animal's leg. Furthermore, the device can determine the direction of propagation of neural activity along the nerve by analyzing the phase of the recorded signals. We believe this technique could be useful for the rapid development of custom-sized nerve interfaces and be applied in implantable therapies that require modulation or monitoring of nerve activity.

4. Experimental Section

Inkjet-Printed 3D Microelectrode Arrays: 3D microelectrodes were printed on a 50 μm thick polyethylene naphthalate (PEN) film (Teonex Q65HA, DuPont Teijin Films, Wilton, UK), using a silver nanoparticle ink (Silverjet DGP 40LT-15C, Sigma-Aldrich, St. Louis, MO, USA) with an inkjet printer (CeraPrinter F-Series, Ceradrop, Limoges, France). Before printing, room temperature Ag nanoparticle ink was sonicated

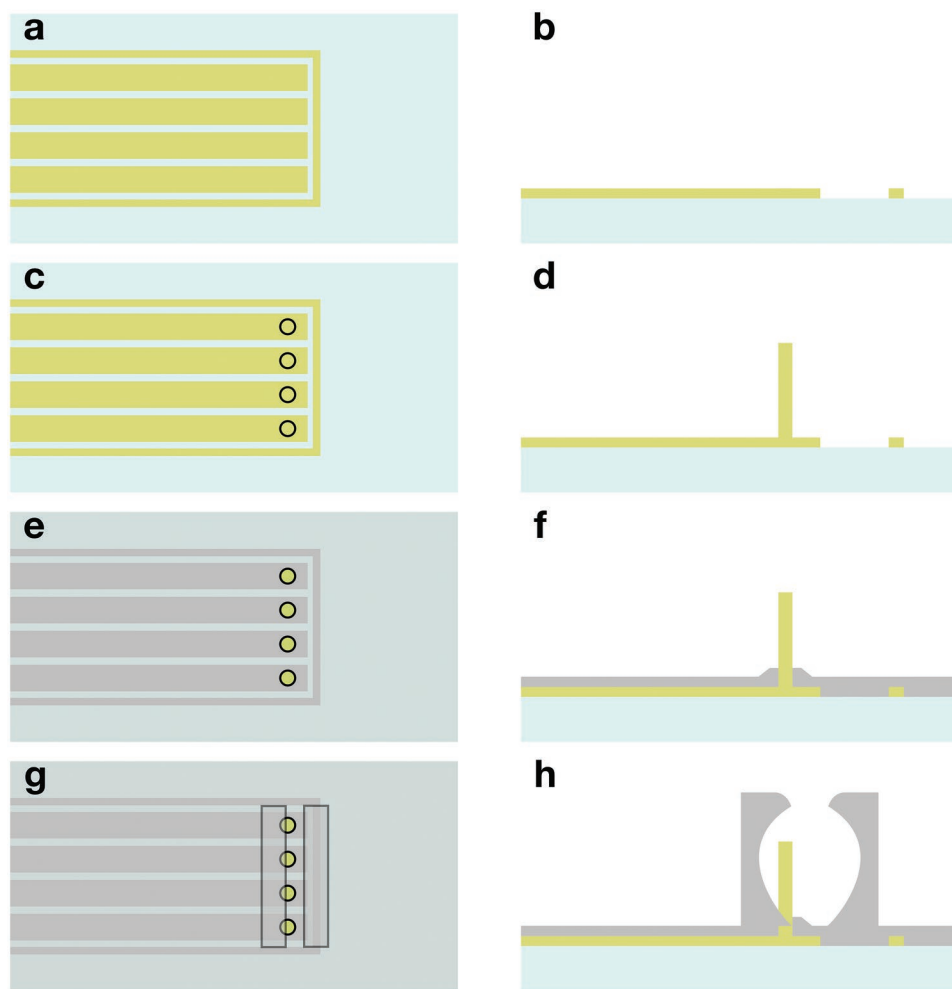


Figure 6. Electrode fabrication process of the proposed cuff electrode. a,b) Printing of the feedline connectors. c,d) Printing of the 3D microelectrodes via successive deposition of Ag nanoparticle ink droplets on top of each other. e,f) Deposition of the insulation layer covering the feedlines. g,h) Fabrication of the 3D nerve cuff via two-photon stereolithography.

(Branson ultrasonic cleaner 5510E-MTH, Branson ultrasonics, Danbury, CT, USA) for 20 min, filtered using a poly(vinylidene fluoride) filter (GD/X, Whatman, Maidstone, UK; pore size: 0.2 μm), and filled into a disposable 1 pL cartridge (DMC-11601, Fujifilm Dimatix, Santa Clara, CA, USA). The waveform applied to the piezoelectric actuator has been previously described.^[41] The sample stage and the nozzle plate were held at 60 and 55 $^{\circ}\text{C}$, respectively.

The feedlines for the 3D microelectrodes were printed with an ejection frequency of 1 kHz, a drop spacing of 40 μm , and an individual Ag nanoparticle droplet diameter of $\approx 60 \mu\text{m}$ on the PEN film (Figure 6a,b). 1000 droplets of Ag nanoparticle ink ($\approx 250 \mu\text{m}$ height) were used to form the 3D microelectrodes using a moving printed head (continuous printing method), with a drop-to-drop time interval of 3.75 s (Figure 6c,d). Once printed, the Ag nanoparticle ink was dried on the sample stage and thermally sintered in a preheated oven at 220 $^{\circ}\text{C}$ for 2 h. In order to not induce thermal stress, the sides of the PEN foil were taped (Kapton tape, VWR, Darmstadt, Germany) to a glass petri dish and slowly cooled down to room temperature after sintering for 2 h.

Printing the Passivation: After sintering the 3D microelectrodes, an ultraviolet (UV) curable acrylate ink (PA-1210-004, JNC Corporation, Tokyo, Japan) was used to passivate the feedlines whilst allowing the 3D microelectrodes to protrude through the insulation layer (Figure 6e,f). Before printing, the UV curable acrylate ink was filtered through a

0.22 μm polyethersulfone (PES) filter (TPP, Trasadingen, Switzerland), loaded into a 1 pL cartridge (DMC-11601, Fujifilm Dimatix, Santa Clara, CA, USA) and covered with Al foil to protect the ink against light.

Individual sensors were placed and held on the printer's substrate holder. In the print layout, a 20 μm spacing around the 3D electrodes was defined to ensure that the electrode structures were not covered in passivation ink. A single nozzle was used with the same waveform previously applied for the Ag nanoparticle ink during the print. The single nozzle was manually aligned with the 3D microelectrodes using the printer's on-board camera. A two-step passivation process was established without any O_2 plasma activation using a heated nozzle plate (40 $^{\circ}\text{C}$) and sample stage (50 $^{\circ}\text{C}$). The first layer comprised of individual droplets of cured acrylate ink (diameter $\approx 50 \mu\text{m}$) spaced evenly with a pitch of 100 μm . Thereafter, a layer of acrylate ink was printed with an ejection frequency of 1 kHz and a drop spacing of 32.5 μm . Lastly, the ink was cured using an inbuilt UV lamp with an approximate dose of 1 J cm^{-2} .

Two-Photon Stereolithographic Cuff Printing and Laser Cutting: All cuffs were designed with Fusion 360 (Autodesk, 2020), exported as STL files, and converted to print job instructions using Describe. The inkjet-printed 3D microelectrodes were aligned and selectively exposed with an erbium-doped femtosecond laser source (center wavelength 780 nm) using Nanoscribe GT Photonics Professional operating in dip-in mode (Figure 6g,h). Power amounted to 150 mW using a 25 \times (NA 0.8)

objective. Cuffs were printed using IP-S resin (all Nanoscribe GmbH, Karlsruhe, Germany).

After printing with the two-photon stereolithographic printer, a 3-axis UV laser marker (MD-U1000C, Keyence, Osaka, Japan) was used to cut the cuff sensor along the already predefined silver outlines. The laser was set to 1.5 kW, with a shutter frequency of 100 kHz, and writing at a speed of 100 mm s⁻¹. The outline was etched with the laser for a total of 100 repetitions. The substrate was aligned and focused using the on-board Keyence software.

Scanning Electron Microscopy: Samples were imaged with a scanning electron microscope (JSM-6060LV, JEOL, Tokyo, Japan). To this end, individual cuff sensors were sputtered with gold using a high vacuum coating system (5×10^{-5} bar, 40 s, 40 mA, approximate film thickness 10 nm; BAL-TEC Med 020, LabMakelaar Benelux BV, Zevenhuizen, The Netherlands). Strips of copper tape and a double-sided carbon pad were used to fix the sensors to the SEM holder to inhibit charge accumulation. Variable magnifications, substrate tilts, and acceleration voltages were used to image the sensors. All captured images were later tilt-corrected using GIMP (Figure 6i–k).

Electrochemical Characterization of Cuff Sensors: Electrochemical impedance spectroscopy was performed to characterize the 3D microelectrodes using a potentiostat (VSP-300, Bio-Logic Science Instruments, Seyssinet-Pariset, France). Locust's saline solution (147 mM NaCl, 10 mM KCl, 4 mM CaCl₂, 3 mM NaOH, and 10 mM HEPES buffer, Sigma Aldrich) was used as the electrolyte.^[44] The measurements were carried out in a two-electrode setup. The individual 3D microelectrodes were set as the working electrode, and either a Pt mesh or another 3D microelectrode was used as a combined counter and reference electrode. No bias voltage was applied against the open circuit potential (E_{oc}) during the experiments. A sinusoidal waveform with an amplitude of 10 mV vs E_{oc} was applied to measure the impedance of the electrodes over a frequency range of 10⁰–10⁵ Hz.

Nerve Interfacing: Adult male and female locusts (*Locusta migratoria*) were used for the in vivo experiments. Since the study was conducted exclusively with locusts (insects), no special permission is required in Germany. All experiments comply with the German laws for animal welfare ("Deutsches Tierschutzgesetz"). Before the surgery, the locusts were anesthetized by cooling them down to ≈ 2 °C for 30 min. Afterward, they were placed ventral side up on a modeling clay bed under a microscope. The cuticle of the metathorax and the air sacs below it were removed to expose the metathoracic ganglion and the N5, a nerve comprising the fibers responsible for the fast extension of the hind tibia. Then, locust's saline solution was applied to the thoracic cavity to prevent the nervous tissue from drying during the procedure. Next, with the aid of micromanipulators, the cuff electrode was approached, and the nerve was inserted into it. The contact pads of the electrodes were interfaced to a 4-pin zero insertion force (ZIF) connector (Würth Elektronik GmbH & Co. KG, Germany). This connector bridged the electrodes to an INTAN RHX control system, using the RHS2116 headset (INTAN Technologies, USA) to stimulate and record activity from the nerve.

The first stimulation protocol consisted of trains of charge-balanced biphasic current pulses of 1 kHz, with an amplitude of 60 μ A and a duration of 500 μ s per phase. Opposite current pulses were applied simultaneously to two microelectrodes every 1 s, and the number of pulses per train was increased from 5 to 20 in steps of 5. For this protocol, the stimuli were driven between every combination of two individual electrodes, one with a leading cathodic phase and the other with a leading anodic phase. The second stimulation protocol consisted of 1 kHz trains of biphasic current pulses with an amplitude of 30 μ A (all other parameters stayed the same). The stimuli were driven between every combination of two pairs of electrodes, one pair with a leading cathodic phase and the other pair with a leading anodic phase. In both protocols, the total stimulation current is preserved (i.e., 1 electrode with 60 μ A or 2 electrodes with 30 μ A at each phase), and the magnitude of the current per phase, cathodic and anodic, was equal at any given time, to drain all the current that was sourced. The elicited movement of the leg for both protocols was recorded on camera, and the tibiofemoral joint angle was estimated using MATLAB (MATLAB 2020b, MathWorks, USA).

Finally, neural activity of the N5 was recorded from all channels @ 30 ksp. The recording setup consisted of the microelectrodes interfacing the nerve on one side of the metathorax, a Pt mesh set as the grounding electrode on the contralateral side, and a Ag/AgCl electrode set as the reference electrode positioned in the abdomen of the subject. To elicit neural activity, two insect pins were inserted at the distal end of the femur separated ≈ 1 mm from each other, and delivered a ≈ 6 ms, 2 V pulse between them every 2 s. The acquired signals were subsequently processed using MATLAB. A second-order high-pass Butterworth filter with a cutoff frequency of 100 Hz was applied in the forward and backward direction, to remove low-frequency noise without phase distortion.

Supporting Information

Supporting Information is available from the Wiley Online Library or from the author.

Acknowledgements

The authors acknowledge funding from the Bavarian State Ministry of Science and the Arts as part of the Bavarian Research Institute for Digital Transformation (bidt) and the Bavarian Research Focus "Herstellung und biophysikalische Charakterisierung von dreidimensionalen Geweben (CANTER)." This work was funded by the Federal Ministry of Education and Research (BMBF) and the Free State of Bavaria under the Excellence Strategy of the Federal Government and the Länder (TUM Innovation Network: NEUROTECH). The authors gratefully acknowledge Petra Schwille and Frank Siedler for generous access to the microfabrication lab at the Max Planck Institute of Biochemistry.

Open access funding enabled and organized by Projekt DEAL.

Conflict of Interest

The authors declare no conflict of interest.

Author Contributions

F.Z., L.G., and A.E. contributed equally to this work. F.Z. and B.W. designed the study. L.G. prepared Figures 2 and 6, F.Z. prepared Figures 1 and 3–5. F.Z. wrote the main manuscript text, with support from L.G., A.E., O.H., and B.W. F.Z. designed the electrode, L.G. and A.E. produced it, with support from H.C.S. and S.S. F.Z. conducted the experiments and processed the data. F.D.D. performed the finite element simulations. F.Z., L.G., and F.D.D. made the Supporting Information Section. All authors reviewed the manuscript and provided critical feedback.

Data Availability Statement

The data that support the findings of this study are available from the corresponding author upon reasonable request.

Keywords

3D printing, implantable electrode, nerve cuff

Received: June 17, 2022

Revised: September 28, 2022

Published online: October 30, 2022

- [1] J. Fan, W. Shan, J. Wu, Q. Wang, *CNS Neurosci. Ther.* **2019**, 25, 1222.
- [2] J. M. Bottomley, C. LeReun, A. Diamantopoulos, S. Mitchell, B. N. Gaynes, *Compr. Psychiatry* **2020**, 98, 152156.
- [3] S. C. Payne, J. B. Furness, O. Burns, A. Sedo, T. Hyakumura, R. K. Shepherd, J. B. Fallon, *Front. Neurosci.* **2019**, 13, 418.
- [4] G. Yao, L. Kang, J. Li, Y. Long, H. Wei, C. A. Ferreira, J. J. Jeffery, Y. Lin, W. Cai, X. Wang, *Nat. Commun.* **2018**, 9, 5349.
- [5] P. Staats, G. Giannakopoulos, J. Blake, E. Liebler, R. M. Levy, *Neuromodulation* **2020**, 23, 784.
- [6] J. A. George, D. T. Kluger, T. S. Davis, S. M. Wendelken, E. V. Okorokova, Q. He, C. C. Duncan, D. T. Hutchinson, Z. C. Thumser, D. T. Beckler, P. D. Marasco, S. J. Bensmaia, G. A. Clark, *Sci. Robot.* **2019**, 4, 2352.
- [7] S. Raspopovic, G. Valle, F. M. Petrini, *Nat. Mater.* **2021**, 20, 925.
- [8] A. Fitchett, S. Mastitskaya, K. Aristovich, *Front. Neurosci.* **2021**, 15, 685872.
- [9] C. J. Bettinger, *Bioelectron. Med.* **2018**, 4, 6.
- [10] S. P. Lacour, J. J. Fitzgerald, N. Lago, E. Tarte, S. McMahon, J. Fawcett, *IEEE Trans. Neural Syst. Rehabilitation Eng.* **2009**, 17, 454.
- [11] T. Boretius, J. Badia, A. Pascual-Font, M. Schuettler, X. Navarro, K. Yoshida, T. Stieglitz, *Biosens. Bioelectron.* **2010**, 26, 62.
- [12] V. Gaillet, A. Cutrone, F. Artoni, P. Vagni, A. M. Pratiwi, S. A. Romero, D. L. Di Paola, S. Micera, D. Ghezzi, *Nat. Biomed. Eng.* **2020**, 4, 181.
- [13] F. Lotti, F. Ranieri, G. Vadalà, L. Zollo, G. Di Pino, *Front. Neurosci.* **2017**, 11, 497.
- [14] S. Lienemann, J. Zötterman, S. Farnebo, K. Tybrandt, *J. Neural Eng.* **2021**, 18, 045007.
- [15] S. Lee, W. Y. X. Peh, N. V. Thakor, S.-C. Yen, C. Lee, in *2017 19th International Conference on Solid-State Sensors, Actuators and Microsystems (TRANSDUCERS)*, IEEE, Kaohsiung, Taiwan **2017**, p. 1730.
- [16] M. A. González-González, A. Kanneganti, A. Joshi-Imre, A. G. Hernandez-Reynoso, G. Bendale, R. Modi, M. Ecker, A. Khurram, S. F. Cogan, W. E. Voit, *Sci. Rep.* **2018**, 8, 16390.
- [17] Y. Shi, R. Liu, L. He, H. Feng, Y. Li, Z. Li, *Smart Mater. Med.* **2020**, 1, 131.
- [18] C. G. Y. Ngan, R. M. I. Kapsa, P. F. M. Choong, *Materials* **2019**, 12, 1927.
- [19] A. Erben, M. Hörning, B. Hartmann, T. Becke, S. A. Eisler, A. Southan, S. Cranz, O. Hayden, N. Kneidinger, M. Königshoff, M. Lindner, G. E. M. Tovar, G. Burgstaller, H. Clausen-Schaumann, S. Sudhop, M. Heymann, *Adv. Healthcare Mater.* **2020**, 9, 2000918.
- [20] K. Lee, D. Yang, S. H. Park, T. W. Lim, R. H. Kim, in *2006 International Symposium on Biophotonics, Nanophotonics and Metamaterials*, IEEE, Hangzhou, China **2006**, p. 8.
- [21] W. F. Gillis, C. A. Lissandrello, J. Shen, B. W. Pearre, A. Mertiri, F. Deku, S. Cogan, B. J. Holinski, D. J. Chew, A. E. White, T. M. Otchy, T. J. Gardner, *J. Neural Eng.* **2018**, 15, 016010.
- [22] J. Jang, J. Kim, Y. C. Kim, S. Kim, N. Chou, S. Lee, Y. Choung, S. Kim, J. Brugger, H. Choi, J. H. Jang, *Adv. Healthcare Mater.* **2019**, 8, 1900379.
- [23] C. Yang, Q. Cao, P. Puthongkham, S. T. Lee, M. Ganesana, N. V. Lavrik, B. J. Venton, *Angew. Chem., Int. Ed.* **2018**, 57, 14255.
- [24] C. A. Lissandrello, W. F. Gillis, J. Shen, B. W. Pearre, F. Vitale, M. Pasquali, B. J. Holinski, D. J. Chew, A. E. White, T. J. Gardner, *J. Neural Eng.* **2017**, 14, 036006.
- [25] C. C. Rowan, O. Graudejus, T. M. Otchy, *Adv. Sci.* **2022**, 9, 2102945.
- [26] T. M. Otchy, C. Michas, B. Lee, K. Gopalan, V. Nerurkar, J. Gleick, D. Semu, L. Darkwa, B. J. Holinski, D. J. Chew, A. E. White, T. J. Gardner, *Nat. Commun.* **2020**, 11, 4191.
- [27] N. Harischandra, A. J. Clare, J. Zakotnik, L. M. L. Blackburn, T. Matheson, V. Dürr, *PLoS Comput. Biol.* **2019**, 15, e1007437.
- [28] F. Rattay, *Neuroscience* **1999**, 89, 335.
- [29] Y. Grinberg, M. A. Schiefer, D. J. Tyler, K. J. Gustafson, *IEEE Trans. Neural Syst. Rehabil. Eng.* **2008**, 16, 572.
- [30] K. Aristovich, M. Donega, C. Fjordbakk, I. Tarotin, C. A. R. Chapman, J. Viscasillas, T.-R. Stathopoulou, A. Crawford, D. Chew, J. Perkins, D. Holder, *J. Neurosci. Methods* **2021**, 352, 109079.
- [31] G. Hoyle, *Proc. R. Soc. London, Ser. B* **1955**, 143, 281.
- [32] M. R. Emad, L. Zeinali, A. Nikseresht, M. Naseri, H. Karimian, *Acta Med. Iran.* **2017**, 55, 496.
- [33] R. G. L. Koh, M. Balas, A. I. Nachman, J. Zariffa, *J. Neural Eng.* **2020**, 17, 016042.
- [34] J.-A. Hoffer, K. Kallesøe, in *Neural Prostheses for Restoration of Sensory and Motor Function* (Eds: J. Chapin, K. Moxon), CRC Press, Boca Raton, Florida, USA **2000**.
- [35] D. Xu, J. Mo, X. Xie, N. Hu, *Nano-Micro Lett.* **2021**, 13, 127.
- [36] P. D. Jones, A. Moskalyuk, C. Barthold, K. Gutöhrlein, G. Heusel, B. Schröppel, R. Samba, M. Giugliano, *Front. Neurosci.* **2020**, 14, 405.
- [37] M. Criado-Gonzalez, A. Dominguez-Alfaro, N. Lopez-Larrea, N. Alegret, D. Mecerreyes, *ACS Appl. Polym. Mater.* **2021**, 3, 2865.
- [38] V. Singh, T. Kumar, *J. Sci.: Adv. Mater. Devices* **2019**, 4, 538.
- [39] M. J. Donahue, C. M. Proctor, X. Strakosas, in *Redox Polymers for Energy and Nanomedicine*, The Royal Society of Chemistry, London **2020**, pp. 488–545.
- [40] F. Zurita, F. Del Duca, T. Teshima, L. Hiendlmeier, M. Gebhardt, H. Luksch, B. Wolfrum, *Sci. Rep.* **2022**, 12, 10864.
- [41] L. Grob, P. Rinklin, S. Zips, D. Mayer, S. Weidlich, K. Terkan, L. J. K. Weiß, N. Adly, A. Offenhäusser, B. Wolfrum, *Sensors* **2021**, 21, 3981.
- [42] S. Stríteský, A. Marková, J. Vítěček, E. Šafaříková, M. Hrabal, L. Kubáč, L. Kubala, M. Weiter, M. Vala, *J. Biomed. Mater. Res.* **2018**, 106, 1121.
- [43] G. Dijk, A. L. Rutz, G. G. Malliaras, *Adv. Mater. Technol.* **2020**, 5, 1900662.
- [44] R. M. Robertson, K. E. Spong, P. Srithiphaphirom, *Sci. Rep.* **2017**, 7, 10297.